

A Numerical Study of the Tip Wake of a Wind Turbine Impeller Using Extended Proper Orthogonal Decomposition

Weimin Wu and Chuande Zhou*

School of Mechanical and Power Engineering, Chongqing University of Science & Technology, Chongqing, 401331, China

*Corresponding Author: Chuande Zhou. Email: c.d.zhou@cqust.edu.cn

Received: 03 March 2020; Accepted: 23 July 2020

Abstract: The behavior of the tip wake of a wind turbine is one of the hot issues in the wind power field. This problem can partially be tackled using Computational Fluid Dynamics (CFD). However, this approach lacks the ability to provide insights into the spatial structure of important high-order flows. Therefore, with the horizontal axis wind turbine as the main focus, in this work, firstly, we conduct CFD simulations of the wind turbine in order to obtain a data-driven basis relating to multiple working conditions for further analysis. Then, these data are studied using an extended Proper Orthogonal Decomposition (POD) algorithm. The quantitative results indicate that the tip vortex in the wake has a complicated spatio-temporal morphological configuration in the higher-order extended POD space. The radial velocity modes obtained are effective and credible, and such reconstructed flow of the tip vortex becomes clearer with the increase of the reconstruction orders. Interestingly, the changes of relatively high-order correlation coefficients are essentially affected by the periodic fusion of tip and central eddies in the wake.

Keywords: Wind turbine; tip vortex; extended POD algorithm; multi-level flow mode

1 Introduction

The sustainable development of energy utilization is a core strategic issue that needs to be solved urgently worldwide, coupled with the increasing shortage of conventional mainstream energy sources such as coal, oil, and natural gas, as well as the growing threat of global warming and climate change. As a clean energy source with good development potential and pollution-free emissions, wind energy is gradually becoming the mainstream energy options in society. For example, in developed countries such as Denmark, Ireland, Portugal, and Germany, the proportion of wind power generation in total power supply in 2019 exceeded 20%, and the highest ratio was close to 50% [1].

In the research of wind power generation and related development, such aerodynamic performance of the wind turbine impeller is a key link of the entire wind energy conversion system. Among them, the flow patterns and change laws of the tip vortex, which is closely related to the aerodynamic shape of the impeller tip, can not only have an important impact on the global aerodynamic characteristics of the wind turbine impeller, and also there is a very close correlation with the internalization and mixing



This work is licensed under a Creative Commons Attribution 4.0 International License, which permits unrestricted use, distribution, and reproduction in any medium, provided the original work is properly cited.

characteristics of the corresponding wake flow field. This further affects the efficiency of the available mechanical energy in the wind energy conversion system and the cycle fatigue life and operating reliability of related equipment systems [2].

In recent years, many researchers at home and abroad have carried out a series of targeted studies on the vortex shedding of wind turbine blades, important correlation features and related control, and made corresponding analysis progress with high credibility and high scientific value. At present, there are mainly three aspects of systematic investigation. Firstly, in the research of vortex shedding of wind turbine blade tips, the experimental measurement study of wind turbine blade tip vortex capture is a basic way to gain insight into the high reliability of the corresponding aerodynamic mechanism, especially for the very complex surface transitions and impingement zones of associated impeller tips, the corresponding detailed feature information is an important basis for analyzing the tip vortex shedding rules [3]. Micallef et al. [4] used the Stereoscopic Particle Image Velocity (SPIV) measurement technique to analyze the flow field at the tip of a 2-blade impeller with a diameter of 2 meters in detail. The results manifested that the tip vortex showed a slight convection trend inside when it fell off. Gao et al. [5] based Particle Image Velocity (PIV) technology to propose a three-window splicing method and analyzed the blade tip vortex flow structures generated by a horizontal axis wind turbine. It is found that there are obvious tip vortex flow characteristics in the wake flow field under different inflow tip speed ratio operating conditions, and as the tip speed ratio increases, the blade-tip vortex core moves radially outward and the center wake range increases. Gupta et al. [6] verified the relevant free vortex wake model based on wind turbine yaw experiments, in which the predicted vortex core location coincides with the experimental data.

Secondly, in the study of important related features of wind turbine blade-tip vortices, such aspect comprises the analysis of changes in tip vortex and its induction characteristics, stability analysis of tip vortex flows, and correlation investigation of blade tip vortex aeroacoustic radiation. Among them, changes in the aerodynamic shape of the tip and the tip speed ratio have been considered as the most direct and sensitive reasons affecting tip flows [7,8]. The stability of the blade tip vortex is mainly reflected in the spiral structure characteristics of its wake flow field, in which the corresponding unstable components need to be quantified and studied in detail at such specified discrete frequencies. The representative work includes experimental and numerical research by Stefan et al. [9–13].

Thirdly, in the survey of vortex system flow control of wind turbine blade tips, this aspect of the study is not only related to the energy loss caused by the tip vortex and the radiated sound pressure level in the wake, and also has an important sensitive effect to the blade tip with periodic fatigue load, and then affects the global structural dynamic response of the impeller. The current investigation conducted by Klimchenko et al. [14–16], indicated that winglet design, tip modification and tip injection can inhibit and improve the formation intensity of the tip vortex system and its corresponding turbulent kinetic energy level in the wake region.

In summary, the current experimental testing ways and CFD methods can only analyzed the series of characteristics of tip vortex, including formation and change as well as acoustic radiation, from a single level of spatial distribution of experimental result and numerical solution of flow. It lacks the ability to fully analyze and effectively identify the important high-order flow space structures for such problems of blade tip vortex. Therefore, in recent research, Scholars [17,18] have begun to try to take advantage of the efficient and hierarchical calculation of Proper Orthogonal Decomposition (POD) that are widely used in intelligent data processing, to study the important flow characteristics in complicated rotating wake of wind turbine. But related aspects of analysis in the wake of wind turbine impeller are still lacking, and systematic exploration on such vortex system change mechanism of tip wake with POD and multi-level studies has almost not been reported, especially for multiple working conditions.

Consequently, in this study a multi-level quantitative analysis of the impeller wake flow field of the S series airfoil wind turbine will be performed using an extended POD algorithm, that can include multiple operating conditions. In Section 2, the basic mathematical models for fluid flow dynamics and the extended POD algorithm with non-temporal parameter are introduced. The corresponding implementation procedure for our study is demonstrated in Section 3. The numerical method is illustrated in detail in Section 4, for which the selection of non-temporal parameter and such 3D wake model of wind turbine impeller are interpreted, respectively. The validation and grid refinement study for such CFD model were carried out in Section 5. The multi-level quantitative analysis of tip wake flow field is presented in Section 6, followed by the results and discussions. Some conclusions are drawn in the last section.

2 Mathematical Model

In this part, the theoretical background of the basic mathematical models for fluid flow dynamics and extended POD algorithm is described as follows.

2.1 Continuity and Momentum Equations for Flows

For such flows in the study without involving heat transfer or compressibility, the CFD solver only solves conservation equations for mass and momentum. The equation for conservation of mass, or continuity equation, can be written as follows

$$\frac{\partial \rho}{\partial t} + \nabla \cdot (\rho \vec{v}) = S_m \quad (1)$$

The Eq. (1) is the general form of the mass conservation equation and is valid for incompressible as well as compressible flows. The source S_m is the mass added to the continuous phase from the dispersed second phase and any other sources. For our research, it can be simplified and given by

$$\nabla \cdot (\vec{v}) = 0 \quad (2)$$

The conservation of momentum in an inertial reference frame for incompressible flows is described by

$$\rho \frac{\partial}{\partial t} (\vec{v}) + \rho \nabla \cdot (\vec{v} \vec{v}) = -\nabla p + \nabla(\hat{\tau}) + \rho \vec{g} + \vec{F} \quad (3)$$

where p is the static pressure, $\rho \vec{g}$ and \vec{F} are the gravitational body force and external body forces, respectively. The $\hat{\tau}$ is stress tensor and given by

$$\hat{\tau} = \mu \left[(\nabla \vec{v} + \nabla \vec{v}^T) - \frac{2}{3} \nabla \cdot \vec{v} I \right] \quad (4)$$

where μ is the molecular viscosity, I is the unit tensor, and the second term on the right hand side is the effect of volume dilation that can be ignored in our study.

2.2 Extended POD Algorithm

The change of such operating parameters of wind turbine impeller is very important for the evolution and related characteristics of the rotating wake flow field. Therefore, it is very necessary to introduce the extended POD algorithm to analyze the wake characteristics that contains the multiple operating conditions, instead of a single operating condition.

The key point to the extended POD algorithm is to use the instantaneous snapshot subsets with different operating parameters to expand the overall sample space. This is convenient for studying the changing

characteristics of wake flow of impeller in non-temporal parameter dimensions. The corresponding overall sample matrix is

$$\mathbf{A} = [\mathbf{a}(c_1) \quad \mathbf{a}(c_2) \quad \cdots \quad \mathbf{a}(c_l) \quad \cdots \quad \mathbf{a}(c_G)] \quad (5)$$

where \mathbf{A} is the overall sample matrix of the extended POD in the non-temporal parameter dimension, and $\mathbf{a}(c_l)$ is flow field sub-sample corresponding to non-time operating parameter value c_l . Among them, G represents the number of sub-sample in the overall array, in which such sub-sample $\mathbf{a}(c_l)$ can be written as

$$\mathbf{a}(c_l) = [\mathbf{a}(\mathbf{x}, t_1, c_l) \quad \mathbf{a}(\mathbf{x}, t_2, c_l) \quad \cdots \quad \mathbf{a}(\mathbf{x}, t_M, c_l)] \quad (6)$$

where M stands for the number of snapshot in the sub-sample at the condition of value c_l , thus, the dimension of overall sample acts as $N \times (M \cdot G)$.

The covariance matrix of the overall sample can be given by [19,20]

$$\mathbf{C}(\mathbf{A}) = \mathbf{A}^T \mathbf{A} \quad (7)$$

According to its features of real symmetric matrix and corresponding non-negative eigenvalues, such can be transformed into solving eigenvalue problems

$$\mathbf{C}(\mathbf{A})\mathbf{H}_m = \lambda_m \mathbf{H}_m \quad (8)$$

where \mathbf{H}_m denotes the correlation coefficient matrix of wake flow mode with extended POD algorithm with the following form

$$\mathbf{H}_m = [h_m(r_1) \quad h_m(r_2) \quad \cdots \quad h_m(r_{M \cdot G})] \quad (9)$$

where r_l acts as the pseudo time-series, for which it has the sequential relationship of time advance at the M th-order flow mode of sub-sample matrix. Its variation presents the approximately periodic change along time history under the setting conditions of the overall matrix.

Therefore, the wake flow mode in the extended non-temporal parameter dimension is defined as

$$\mathbf{A}_m(\mathbf{x}) = \frac{1}{M \cdot G \cdot \lambda_m} \sum_{l=1}^{M \cdot G} h_m(r_l) \cdot \mathbf{A}(\mathbf{x}, r_l) \quad (10)$$

where λ_m is such eigenvalue corresponding to wake flow mode of overall array, and the \mathbf{x} represents the space discrete vector of numerical computation.

In the light of such information content levels of wake flow modes, the reconstructed form of the reduced-order wake flow field is given by

$$\mathbf{A}(\mathbf{x}, r_l) \approx \bar{\mathbf{A}}(\mathbf{x}, r_l) = \sum_{m=1}^{NT} c_A(r_l, m) \cdot \mathbf{A}_m(\mathbf{x}) \quad (11)$$

where NT is the truncation order of reconstruction of wake flow, and $\bar{\mathbf{A}}(\mathbf{x}, r_l)$ is such approximately reconstructed solution at the pseudo time of r_l .

The corresponding reconstruction error of wake flow at r_l can be written as

$$\mathbf{e}(\mathbf{A})_{r_l} = 100 \cdot |\bar{\mathbf{A}}(\mathbf{x}, r_l) - \mathbf{A}(\mathbf{x}, r_l)| \bigg/ \sum_{n=1}^N \|\mathbf{A}(\mathbf{x}(n), r_l)\|_2 \quad (12)$$

where $\mathbf{e}(\mathbf{A})_{r_l}$ is named as the global reconstruction error vector to represent the accuracy of the whole wake flow. Among them, N stands for the number of node for performing such spatial dispersion.

3 Implementation Procedure

The extended POD analysis of the wind turbine wake flow field is essentially an expansion of the multi-mode dimension with the different high information content flow field results under changing operating conditions. The specific implementation procedure is shown in Fig. 1.

According to the presentation in Fig. 1, it is shown that the first three steps (above) are a set of flow information of multiple working conditions, and the next three steps (below) are multi-level study of wake flow of wind turbine.

Among such procedure, the extraction and conversion of basic CFD data are completed through a self-developed data interface program, and the specific situation is manifested in Fig. 2.

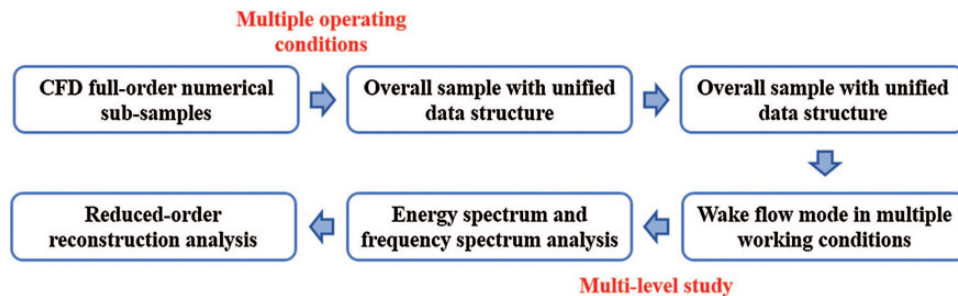


Figure 1: Implementation of wake flow field with extended POD algorithm

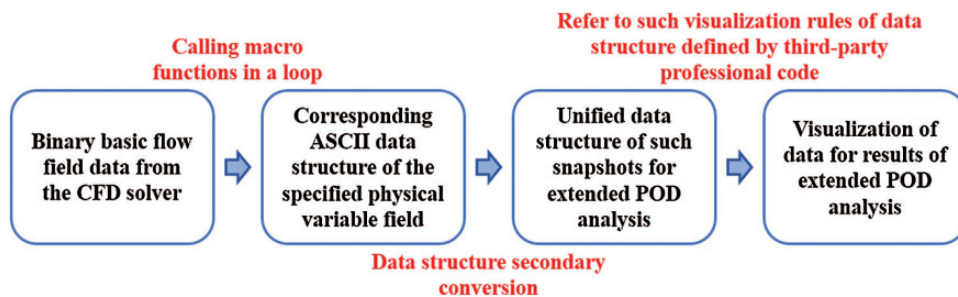


Figure 2: Logical function of the self-developed data interface program

4 Numerical Method

4.1 Selection for Non-Temporal Parameter

The tip speed ratio κ is a very important parameter in the aerodynamic design and optimization of wind turbine, which is very closely to the energy conversion efficiency of the working impeller and the related acoustic radiation characteristics. Therefore, this parameter is selected here as a non-time parameter in the extended POD analysis, and is defined as

$$\kappa = \frac{v}{V} = \frac{2\pi Rn}{60V} \quad (13)$$

where R is the sweep radius of impeller, and n denotes the rotational angular velocity, and v stands for linear velocity of blade tip, as well as V incoming wind Speed of design.

The change in the tip speed ratio κ of the wind turbine impeller is given as

$$\mathbf{E}\mathbf{V} = [\kappa_1 \quad \kappa_2 \quad \cdots \quad \kappa_{l+1} \quad \cdots \quad \kappa_G] \quad (14)$$

where $G = 13$ is the total number of different tip speed ratios in the CFD study, and κ_{l+1} as

$$\kappa_{l+1} = 4.0 + 0.25 \cdot l \quad (15)$$

where $l = 0, 1, 2, \cdots, G - 1$, and it is worth noting that $\kappa_7 = 5.5$ denotes the tip speed ratio of design of wind turbine, represented by the symbol κ_s .

According to formula (13), the rotational speed of wind turbine impeller corresponding to the calculated tip speed ratio can be obtained

$$\mathbf{E}\mathbf{n} = [n_1 \quad n_2 \quad \cdots \quad n_{l+1} \quad \cdots \quad n_G] \quad (16)$$

where the design rotational speed $n_s = n_7$ is about 750.3 r/min.

4.2 Tip Wake Numerical Model of Wind Turbine

The study work will adopt the S series airfoil wind turbine impeller developed by our research group, and related design parameters are listed in Tab. 1.

Table 1: Design parameters for the wind turbine of S series airfoil

Design parameter	Value
Blade number	3
Impeller diameter	1.4 m
Blade tip chord length	0.04 m
Average ratio of span to chord	4.22
blade tip twist	5.8 deg
Rated output power	300 w
Design wind speed	10 m/s
Starting wind speed	3 m/s

According to the characteristic airfoil sections at 20 different local radius and corresponding design twist angles, we generate a solid model of the S series airfoil wind turbine impeller, shown in Fig. 3.

The area layout plan of the 3D wake numerical model is shown in Fig. 4. The rotation center axis is set to the x-axis, and the wake flow direction is the positive direction of x-axis.

We obtain the corresponding rotation encryption area through a Boolean operation between the body-fitting cylindrical area and the impeller solid model, and the cylinder radius of the wake encryption area is consistent with the rotation encryption part to facilitate such subsequent meshing. After a series of verifications of grid independence in space and time, we accomplish a CFD numerical calculation model of the impeller wake flow field, illustrated in Fig. 5.

The radius of the overall cylindrical calculation area is set to 5 times the radius of the impeller sweep surface, which is 3.5 m, to avoid the influence of non-physical interface at the peripheral boundary of the CFD model. The overall cylindrical calculation area has a length of 9 m, and the length of the wake capture area and the radius of the grid encryption area are 6.25 m and 1.1 m, respectively. The encrypted

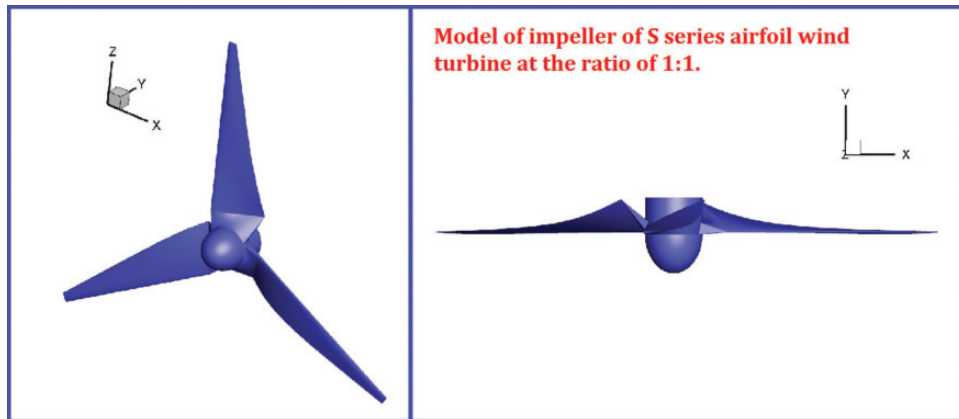


Figure 3: Model of impeller of S series airfoil wind turbine

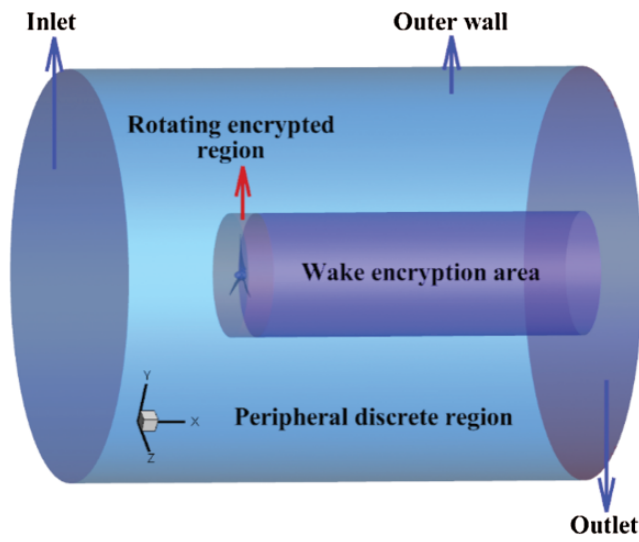


Figure 4: Area layout in CFD model of wake of wind turbine impeller

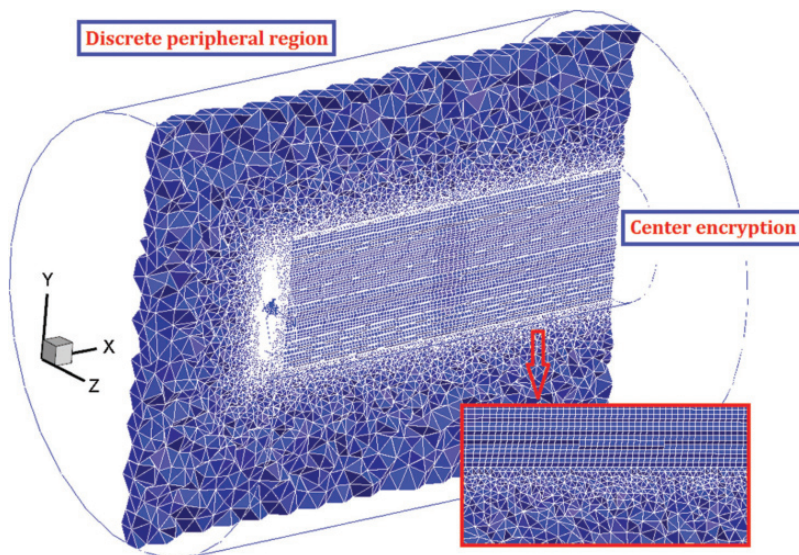


Figure 5: Meshing in CFD model of wake of wind turbine impeller

mesh of the impeller body-fitting region and the center wake region uses such tetrahedral and prism elements to achieve spatial dispersion, respectively. The total number of discrete elements in the CFD wake model is approximately 3.89 million. The flow flux information between the rotating area and the peripheral non-rotating area is transmitted using the sliding mesh model.

The sliding mesh model adopted here is a special case of general dynamic mesh motion wherein the nodes move rigidly in a given dynamic mesh zone. Additionally, multiple cells zones are connected with each other through non-conformal interfaces. As the mesh motion is updated in time, the non-conformal interfaces are likewise updated to reflect the new positions each zone. It is important to note that the mesh motion must be prescribed such that zones linked through non-conformal interfaces remain in contact with each other.

In our numerical calculations, the CFD solver uses a control-volume-based technique to convert a general scalar transport equation to an algebraic equation that can be solved numerically. This control volume technique consists of integrating the transport equation about each control volume, yielding a discrete equation that expresses the conservation law on a control-volume basis.

This is demonstrated by the following equation written in integral form for an arbitrary control volume as follows

$$\int_V \frac{\partial \rho \phi}{\partial t} dV + \oint \rho \phi \vec{v} \cdot d\vec{A} = \oint \Gamma_\phi \nabla \phi \cdot d\vec{A} + \int_V S_\phi dV \quad (17)$$

where ϕ is a scalar quantity, \vec{A} is surface area vector, and Γ_ϕ denotes diffusion coefficient for ϕ , and S_ϕ as source of ϕ per unit volume.

The solution formulation is implicit for promoting such computing efficiency, which cooperates with settings for such pressure-velocity coupling scheme SIMPLE. In the transient computing advance, the early stage uses the First Order Implicit format to achieve stable iterative convergence. In the later period, the Second Order Implicit format is used to accelerate the convergence speed for each working condition.

The turbulent flows are characterized by eddies with a wide range of length and time scales. The mean flow and such dissipation of turbulence kinetic energy are both affected by the largest eddies and smallest ones. In Large Eddy Simulation (LES) chosen here, the large eddies are resolved directly, while small eddies are modeled. Therefore, LES falls between Direct Numerical Simulation (DNS) and Reynolds Averaged Navier-Stokes (RANS) models in terms of the fraction of the resolved scales.

The subgrid-scale turbulence models of LES employ the Boussinesq hypothesis to compute the subgrid-scale turbulent stresses

$$\tau_{ij} - \frac{1}{3} \tau_{kk} \delta_{ij} = -2\mu_t \bar{S}_{ij} \quad (18)$$

where μ_t is the subgrid-scale turbulent viscosity. The τ_{kk} is such isotropic part of the subgrid-scale stresses and can be added to the filtered static pressure term. Such \bar{S}_{ij} is the rate-of-strain tensor for the resolved scale defined by

$$\bar{S}_{ij} = \frac{1}{2} \left(\frac{\partial \bar{u}_i}{\partial x_j} + \frac{\partial \bar{u}_j}{\partial x_i} \right) \quad (19)$$

The subgrid-scale turbulent flux of a scalar, ϕ , is modeled using a subgrid-scale turbulent Prandtl number by

$$q_j = -\frac{\mu_t \partial \phi}{\sigma_t \partial x_j} \quad (20)$$

where q_j is the subgrid-scale flux.

The Smagorinsky-Lilly model is applied here, in which the eddy-viscosity is modeled by

$$\mu_t = \rho L_s^2 |\bar{S}| \quad (21)$$

where L_s is the mixing length for subgrid scales and $|\bar{S}| = \sqrt{2\bar{S}_{ij}\bar{S}_{ij}}$. In our study, is computed using

$$L_s = \min(\kappa d, C_s \Delta) \quad (22)$$

where κ is the von Kármán constant, d is the distance to the closest wall, C_s is the Smagorinsky constant, and Δ is the local grid scale. In this study, Δ is computed according to the volume of the computational cell using

$$\Delta = V^{1/3} \quad (23)$$

Lilly derived a value of 0.23 for C_s for homogeneous isotropic turbulence in the inertial subrange. However, a C_s value of around 0.1 has been found to yield the best results for a wide range of flows, and is the value used in our research.

We set the inlet and outlet boundaries of the CFD model as the velocity-inlet and pressure-outlet, separately. This walls and ambient temperature are both set to 300 K, in which we specify a no-slip condition at the walls for the CFD wake model. The wall roughness constant is set to 0.35 and the roughness height is considered to be zero.

According to formulas (14)–(16), the transient time step for 1 *deg* rotation is

$$\Delta T_{n_{l+1}} = \frac{1}{6 \cdot n_{l+1}} \quad (24)$$

For the design tip speed ratio conditions, $\Delta T_{n_s} = \Delta T_{n_{l+1}}$, which is about $2.22 \times 10^{-4} s$. we will firstly perform the transient numerical advance with at least 10 revolutions to obtain such stable transient numerical calculation results. The convergence standard of continuity residual can be set as 1×10^{-3} in the early stage, and it is set to 5×10^{-4} later. After all the required working conditions have been calculated with convergence in stability, and then the wake flow of each working condition advances and rotates 1 revolution according to the original time step. we save transient simulation data of flow field parameter every 5 time steps, and there are 60 snapshots at each working condition, corresponding to all working conditions of 60×13 .

The characteristic plane of the tip wake flow field is selected, shown in Fig. 6, to reflect the characteristics and changes of the corresponding tip vortex structures. Additionally, the distribution of the radial velocity field can better characterize the changes of tip vortex in the wake, therefore, we choose it as the parameter field for such extended POD analysis.

5 Validation and Grid Refinement Study for the CFD Model

In order to verify the effectiveness of the calculation model and improve its calculation efficiency, a validation of the related numerical results and a grid refinement study have been carried out. In Fig. 7, the results of this experimental measurement and such corresponding numerical calculation are presented for the overall mechanical effects of the wind turbine impeller.

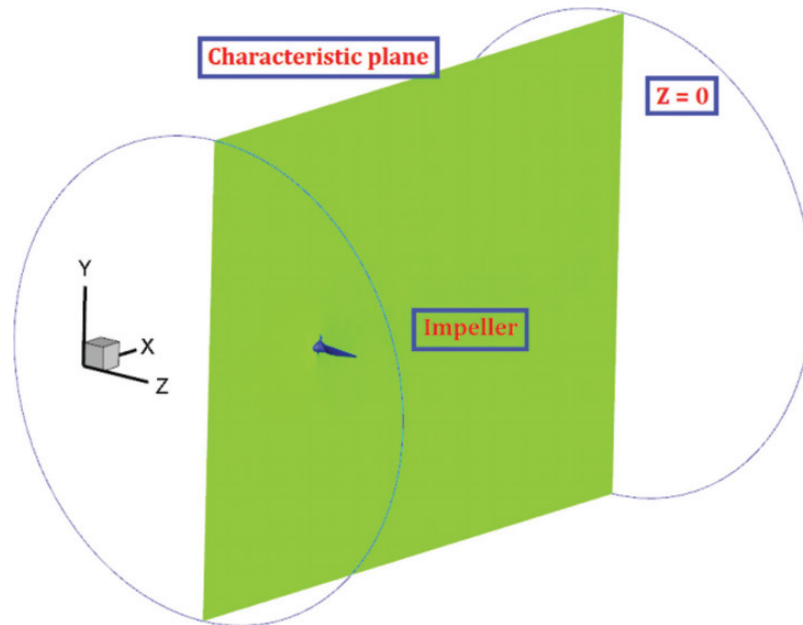


Figure 6: Characteristic plane in CFD wake model

According to Fig. 7a, the axial force integration on the impeller surface shows the characteristic of periodic variation of convergence in time progress, and the result of this numerical calculation is in good agreement with the experimentally measured data in terms of variation. Because the sampling frequency of the experimental measurement is higher than the numerical calculation, the former shows a more intensive data curve.

According to Fig. 7b, the axial torque integration on the impeller surface manifests similar changes to such axial force integration above-mentioned. It is worth noting that the axial torque integration is more sensitive to aerodynamics disturbances. Therefore, here, we choose the average value of the periodic fluctuations of the axial force integration as the reference basis for studying such grid refinement. The specific situation is shown in Fig. 8 below.

Based on the results in Fig. 8, the difference between the calculated value and the experimental measurement is decreasing for the average axial force, as the number of overall grids increases. An inflection point of this smooth approach is approximately located in the number of 3.89 million, which corresponds to the CFD grid model we use in the follow-up. Therefore, the above research indicates that the CFD model we adopt is reasonable, which can save computing resources to a certain extent while ensuring the validity of the calculation.

6 Results of Extended POD Analysis in Tip Wake Flow

In this section, the radial velocity modes are discussed, especially for tip vortex. The effectiveness and accuracy are evaluated by the corresponding reconstructed flow field with such associated error analysis, and the related energy spectrum and frequency characteristics have been studied.

6.1 Radial Velocity Modes of Wake Flow

The radial velocity modes of wake flow under different tip speed ratios and $z_0 = 15$, is manifested in Fig. 9. The z_0 represents the same sequence number of snapshot in each working condition.

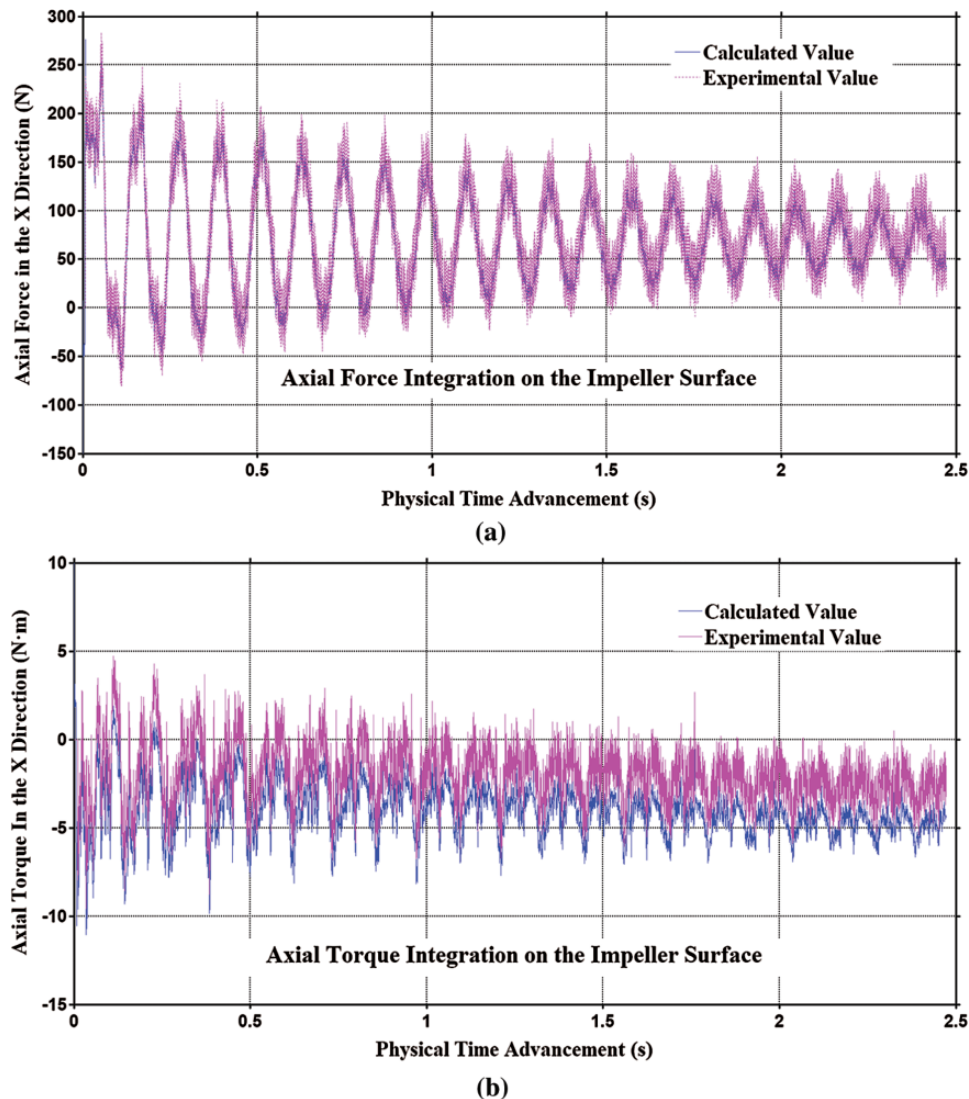


Figure 7: Integration of mechanical quantity for the impeller surface. (a) Variation history of axial force and (b) Variation history of axial torque

According to Fig. 9, The 1st-order radial velocity flow mode of characteristic plane of overall sample presents a very symmetrical high flow gradient morphology with radial inward. During the backward propagation of the wake vortex, it appears as a central vortex without tip vortex characteristics. For the wake far field, an approximately symmetrical high gradient flow-affected area is observed, which is likely to affect the flow of the tip vortex.

The 2nd, 3rd, and 4th modes of the wake flow show the fused evolutionary characteristics of the tip vortex and the central vortex. The morphological characteristics of the blade tip vortex gradually become apparent with the increase of the mode order. The fusion propagation effect between tip vortex and central vortex is further enhanced for the modes from 5th to 8th order, and the spatial symmetry along the positive direction of the x axis is gradually detailed. In the 9th and 10th mode of characteristic plane, the further fusion of the tip vortex system has developed, and they both show the characteristics of outward migration along the radial direction, which shows the corresponding law approximating the overall

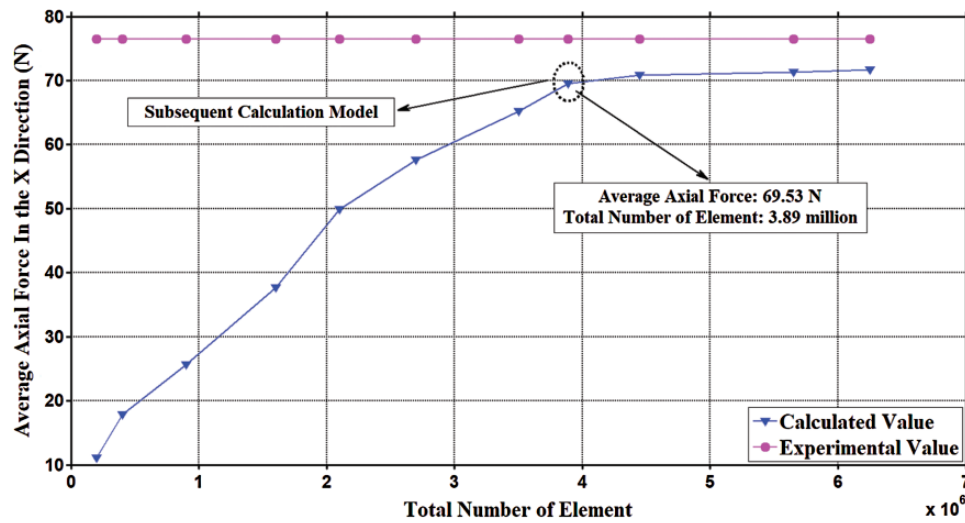


Figure 8: Grid refinement using such average axial force in the X direction

motion of the blade tip vortex. It indicates that there are important flow characteristics in high-order space, and the hierarchical distribution law of the corresponding feature space needs further investigation. Furthermore, the outer region of the far-field wake displays the opposite orthogonal distribution.

It demonstrates that such tip vortex of the wake of the wind turbine have more complicated and obvious spatio-temporal morphological characteristics in such relatively higher-order extended POD space.

6.2 Wake Flow Reconstruction with Extended POD Modes

The numerical results of full-order CFD of radial velocity field, and corresponding reconstruction and error morphology at such design tip speed ratio with $z_0 = 35$, are shown in Figs. 10 and 11, individually.

In the light of Figs. 10 and 11, the reconstruction of first 3 order modes reflects the main central vortex morphology of the wake and radial velocity gradient distribution around such impeller. However, the flow pattern of the blade tip vortex structure is not clearly manifested. The reconstructed flow characteristics of the tip vortex become clearer and the characteristic information of the central vortex is refined, with the increase of the reconstruction orders.

Among them, the corresponding reconstruction maximum error decreased from 33.7% in the first 3 orders to 3.2% in the first 36 orders. The relatively high errors mainly distribute in the local area where the tip vortex and the central vortex are located. The details are shown in Figs. 10a–10d. When the reconstruction order used is the first 72 orders, the corresponding reconstruction maximum error has been reduced to 2.15%.

Consequently, the results above illustrates that the radial velocity modes we obtain are effective and credible, and the relatively high-order flow of the impeller wake is mainly concentrated in the tip vortex and central vortex regions.

6.3 Analysis of Energy Spectrum and Frequency Characteristics

The energetic distribution of wake flow mode at such characteristic plane for first 300 orders, with cumulative and single-order information, are displayed in Fig. 12.

According to the analysis of the characteristics in Fig. 12, the highest energy content in the radial flow of the overall sample is the 1st-order flow mode, which is more than 14%. The cumulative energy content of the first 36 orders and the first 72 orders are about 65.3% and 85.2%, respectively. As the number of order

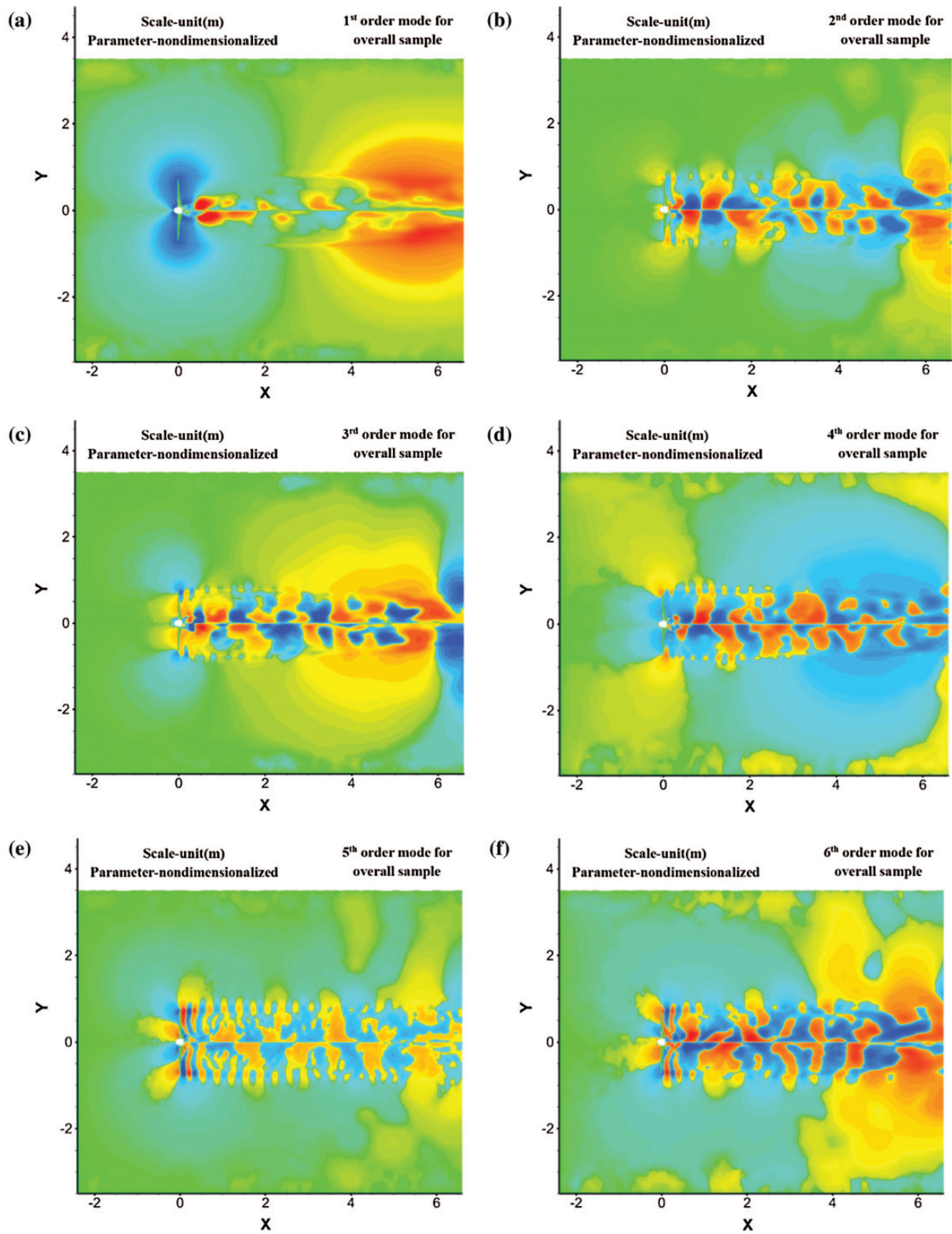


Figure 9: (continued)

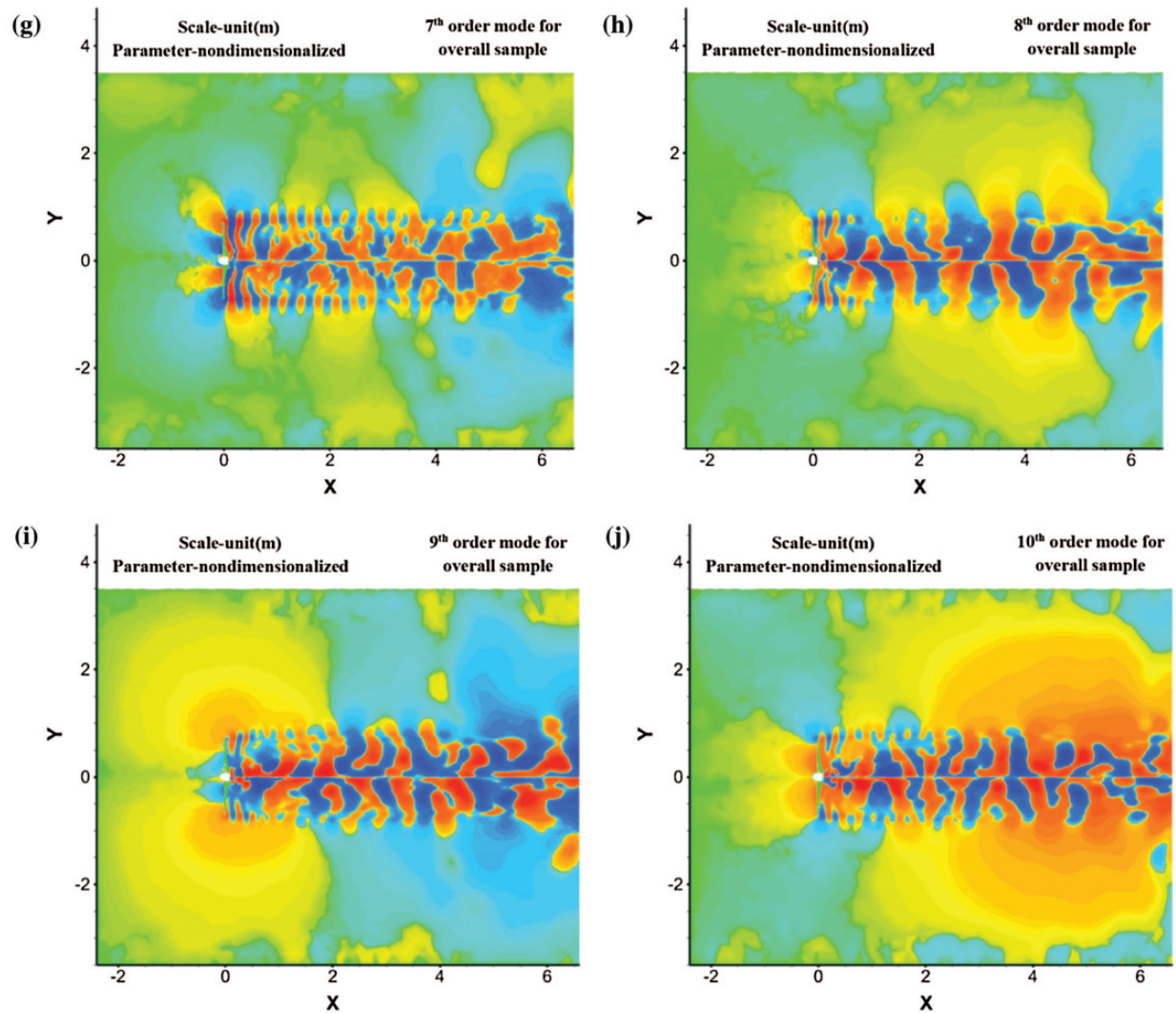


Figure 9: Radial velocity modes of overall sample. (a) 1st order mode, (b) 2nd order mode, (c) 3rd order mode, (d) 4th order mode, (e) 5th order mode, (f) 6th order mode, (g) 7th order mode, (h) 8th order mode, (i) 9th order mode and (j) 10th order mode

increases, the corresponding proportion of radial flow single-order energy content gradually decreases. For the energy content of the first 6 modes, each of them is above 2%, and in the first 18 modes each energy content is still higher than 1%. Therefore, it indicates that in the reconstruction of the wake flow field of the wind turbine, it is of little significance to study the flow modes at excessively high orders.

The correlation coefficient corresponding to the wake flow mode in the overall sample is a pseudo time series, therefore, the significance of its spectral characteristics is mainly reflected in the corresponding sequence of sub-sample data. Fig. 13 shows the spectral characteristics of the first 9 order correlation coefficients of the radial flow mode in the condition of the design tip speed ratio.

The peak of the correlation coefficient of the first-order mode appears at the 0 frequency position, and its peak value is higher than that of the other orders, indicating that this order mainly reflects the overall average displacement of radial flow. The 2nd and 3rd order modes are the situations with the highest energy levels except the 1st order mode, and the corresponding peak frequency is 12.51 Hz that is the fundamental

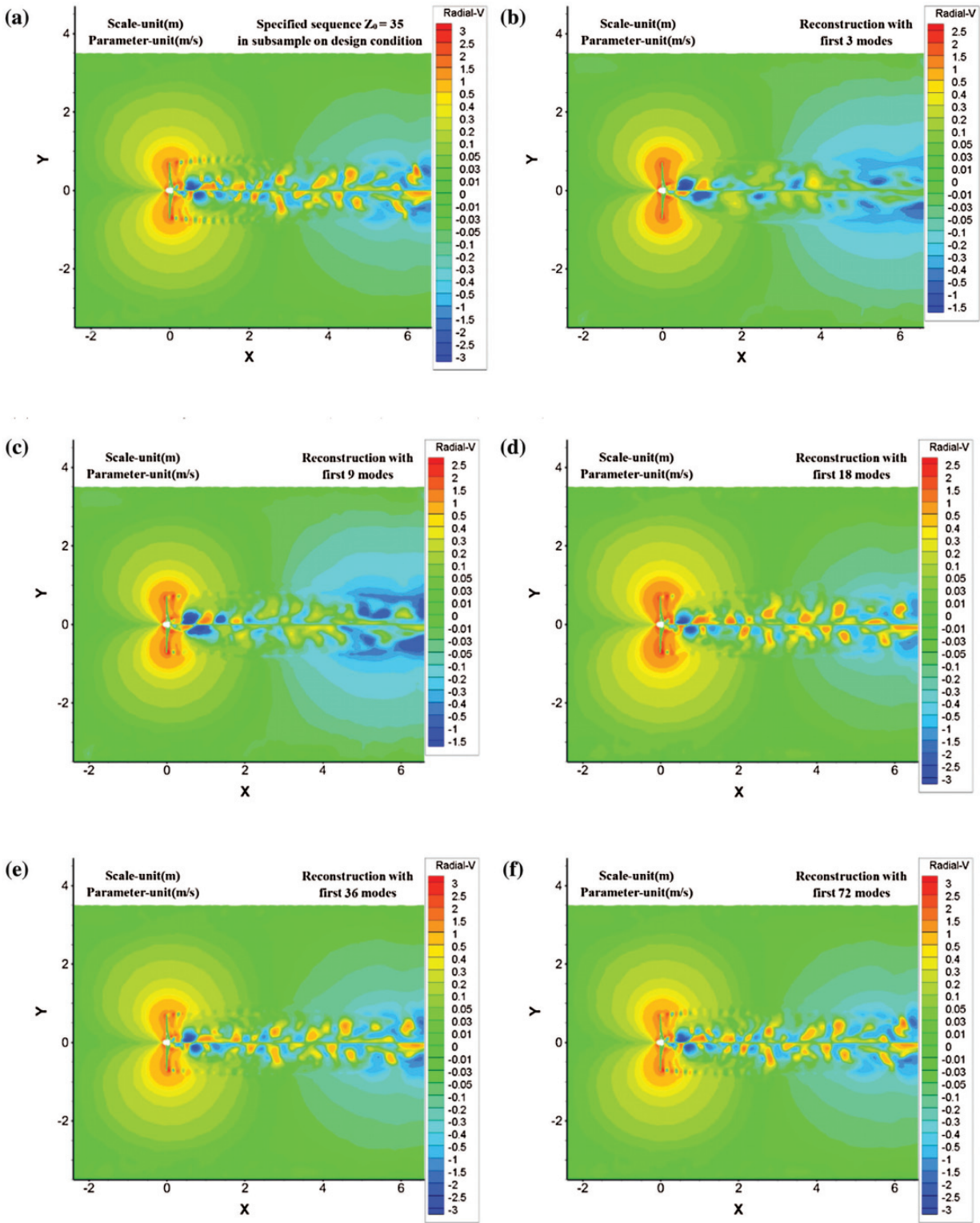


Figure 10: Full-order numerical solution and reconstruction solutions at specified transient time for radial velocity. (a) Radial velocity distribution (CFD), (b) First 3 orders reconstruction, (c) First 9 orders reconstruction, (d) First 18 orders reconstruction, (e) First 36 orders reconstruction and (f) First 72 orders reconstruction

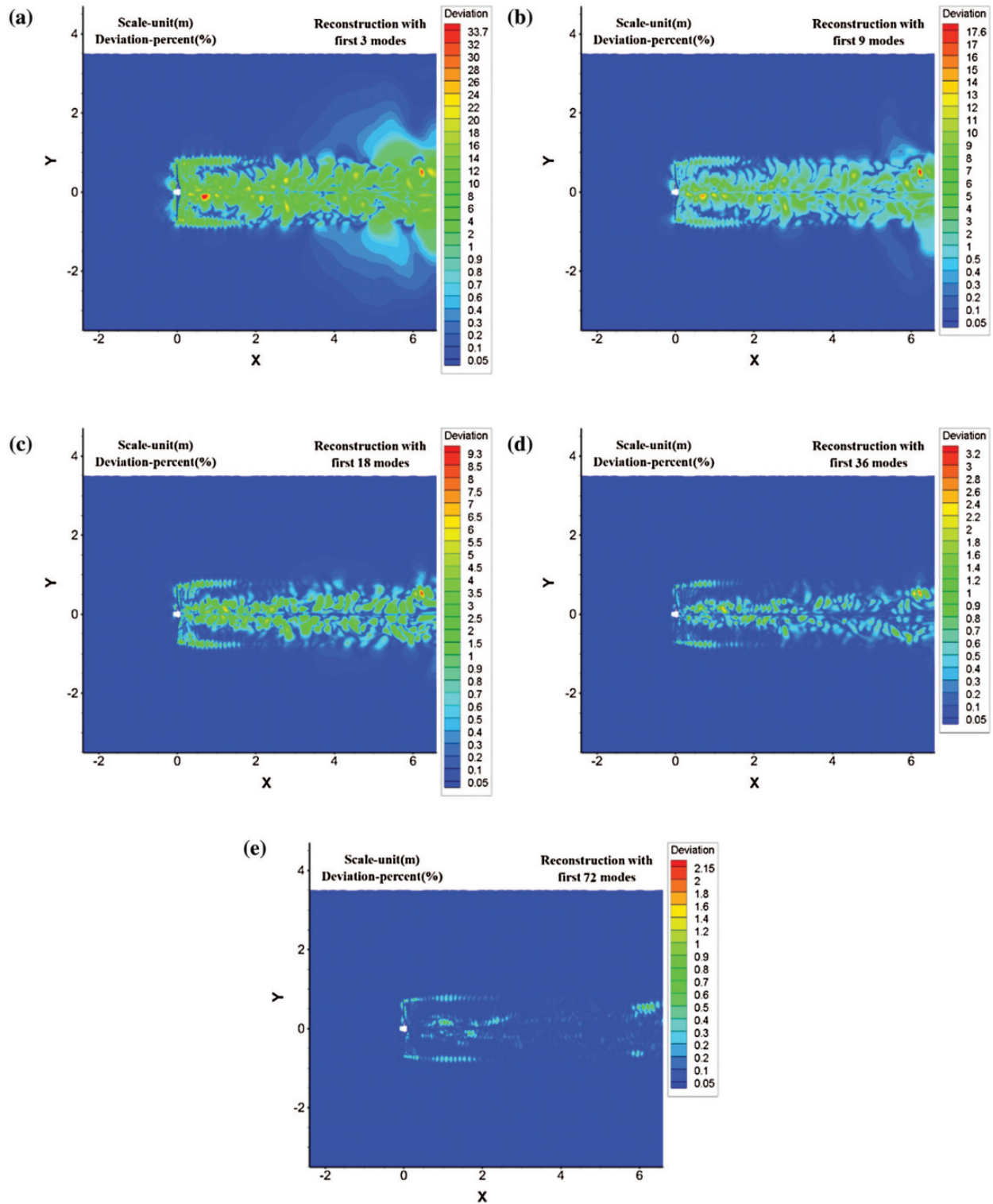


Figure 11: Reconstruction solution error of characteristic plane for radial velocity. (a) First 3 orders reconstruction error, (b) First 9 orders reconstruction error, (c) First 18 orders reconstruction error, (d) First 36 orders reconstruction error and (e) First 72 orders reconstruction error

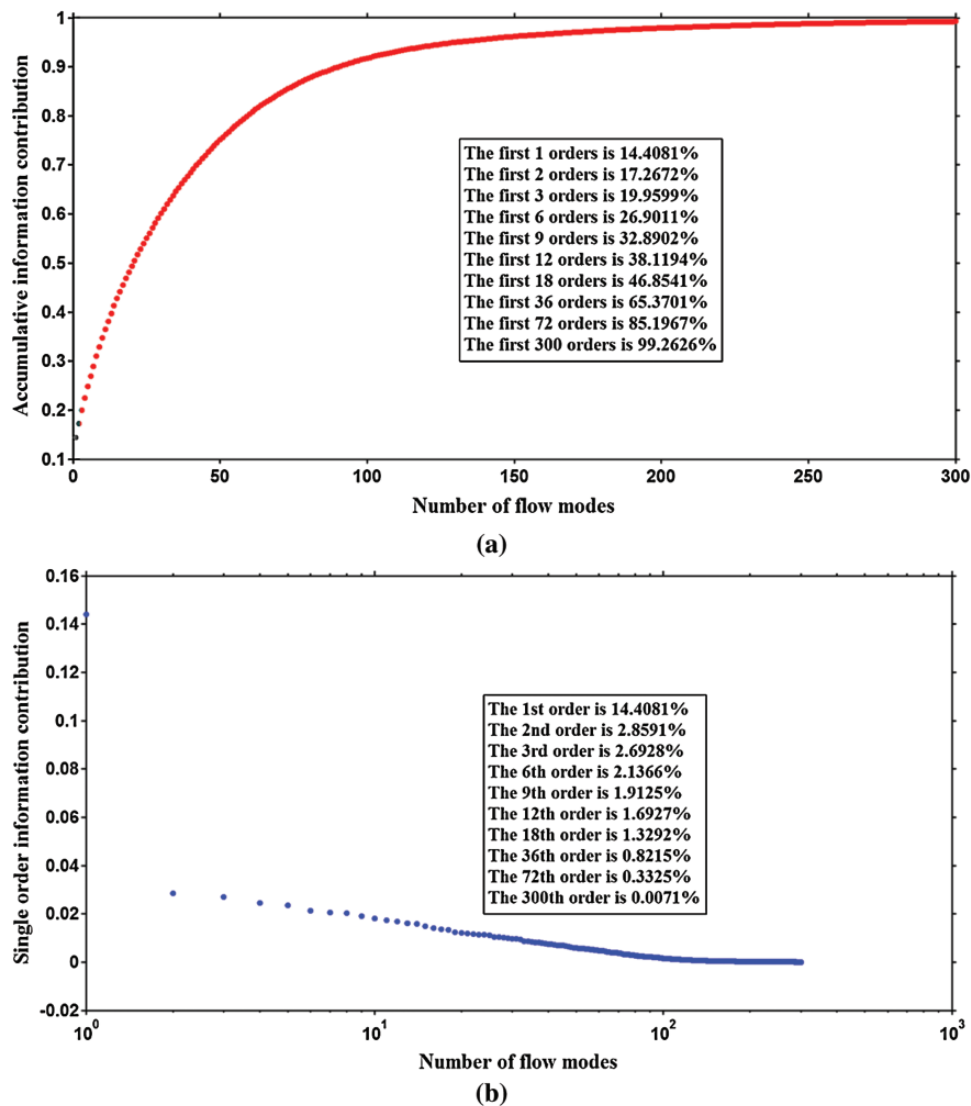


Figure 12: Energy spectrum characteristics at such characteristic plane for radial velocity. (a) Cumulative energetic contribution of the first 300 radial velocity modes and (b) Single-order energetic contribution of the first 300 radial velocity modes

frequency of the rotating wake flow field. The 4th and 5th order flow modes have a peak frequency of 37.52 Hz, which is three times the fundamental frequency, just corresponding to the 3-blade geometric layout of the wind turbine impeller.

The 6th and 7th order wake modes have a peak frequency of 25.01 Hz, which is 2 times the fundamental frequency, and the corresponding 8th and 9th order modes have a peak frequency of 6 times the base frequency of 75.03 Hz. Such change features of relatively high-order correlation coefficients corresponding to the flow modes are mainly affected by the spatio-temporal periodic fusion of the wake tip vortex and central vortex, which is consistent with the modal space distributions shown in Figs. 9f–9i. Meanwhile, the amplitudes of the correlation coefficients of different flow modes are gradually decreasing in pairs, with the increasing of the extended POD spatial order, and the magnitude of the reduction in amplitude is decreasing. It reflects a change rule with respect to multi-level influence.

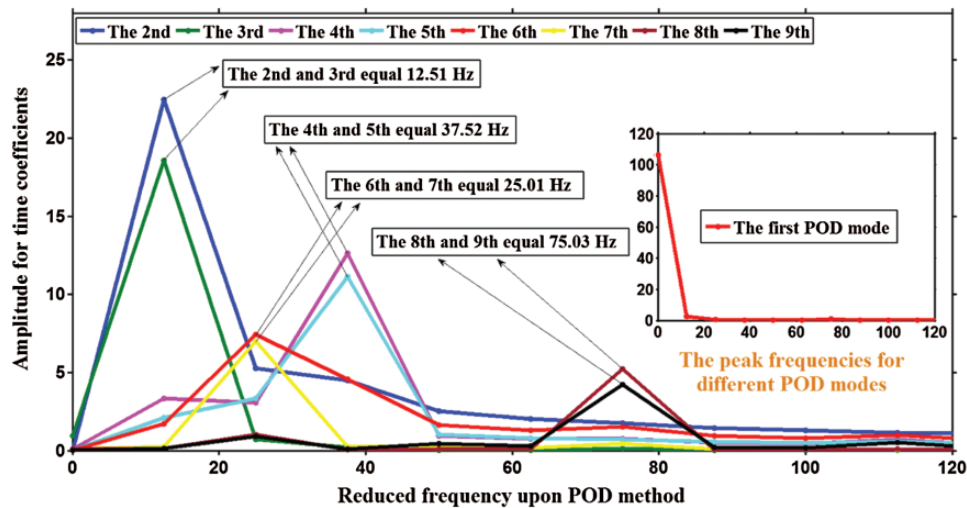


Figure 13: Spectral characteristics of Extended POD correlation coefficients at design tip speed ratio

Additionally, the spectral characteristics of the modal correlation coefficients in the other operating conditions are generally similar to such design operating condition.

7 Conclusions

In this paper, the tip wake field of S series airfoil wind turbine with multiple working conditions are studied at multi-level modal space for wake structures and related quantitative information, using extended POD algorithm. From this research, the following conclusions can be drawn:

1. The tip vortex in the wake of impeller has more complicated and obvious spatio-temporal morphological characteristics at the relatively higher-order extended POD space.
2. The radial velocity modes by the extended POD algorithm are effective and credible, and the reconstructed flow characteristics of the tip vortex become clearer, with the increase of the reconstruction orders.
3. The cumulative energy content of the first 36 orders and the first 72 orders are about 65.3% and 85.2%, respectively, and it is almost no significance to study the flow modes at excessively high orders for wake flow of wind turbine.
4. The change feature of relatively high-order correlation coefficient is mainly affected by the periodic fusion of tip and central eddies in the wake.

Acknowledgement: We sincerely thank the key laboratory of wind and solar power energy utilization technology ministry of education in China.

Funding Statement: This work was supported by the PhD Start-up Fund from Chongqing University of Science and Technology (No. 181903017), the Key R&D Project from Science and Technology of Chongqing (No. cstc2018jszx-cyztzx0003) and the Key R&D Project from Science and Technology of Chongqing (No. cstc2018jszx-cydz0092).

Conflicts of Interest: The authors declare that they have no conflicts of interest to report regarding the present study.

References

1. Gronholt-Pedersen, J. (2020). Denmark sources record 47% of power from wind in 2019. <https://www.yahoo.com/news/denmark-sources-record-47-power-093459131.html>.
2. Frulla, G., Torino, P., Visone, M., Energia, A., Lappa, M. (2015). A practical engineering approach to the design and manufacturing of a mini kw blade wind turbine: definition, optimization and CFD analysis. *Fluid Dynamics & Materials Processing*, 11(3), 257–277.
3. Xiao, J. P., Wu, J., Chen, L., Shi, Z. (2011). Particle image velocimetry (PIV) measurements of tip vortex wake structure of wind turbine. *Applied Mathematics and Mechanics*, 32(6), 729–738. DOI 10.1007/s10483-011-1452-x.
4. Micallef, D., Akay, B., Ferreira, C. S., Sant, T., Bussel, G. (2014). The origins of a wind turbine tip vortex. *Journal of Physics: Conference Series*, 555, 012074. DOI 10.1088/1742-6596/555/1/012074.
5. Gao, Z., Wang, J., Dong, X., You, Z. (2013). Multiwindows PIV experiment on the tip vortex of horizontal axis wind turbine. *Journal of Engineering Thermophysics*, 34(2), 258–261.
6. Gupta, S., Leishman, J. G. (2006). Validation of a free-vortex wake model for wind turbines in yawed flow. *The 44th AIAA Aerospace Sciences Meeting and Exhibit*, 389, pp. 1–15, Reno, Nevada.
7. Kimura, K., Tanabe, Y., Aoyama, T., Matsuo, Y., Arakawa, C. (2016). CFD simulations of a wind turbine for analysis of tip vortex breakdown. *Journal of Physics: Conference Series*, 749, 012013. DOI 10.1088/1742-6596/749/1/012013.
8. Ali, A., Chowdhury, H., Loganathan, B., Alam, F. (2015). An aerodynamic study of a domestic scale horizontal axis wind turbine with varied tip configurations. *Procedia Engineering*, 105, 757–762. DOI 10.1016/j.proeng.2015.05.067.
9. Ivanell, S., Mikkelsen, R. F., Jens, N. S., Henningson, D. (2015). Stability analysis of the tip vortices of a wind turbine. *Wind Energy*, 13(8), 705–715. DOI 10.1002/we.391.
10. Lignarolo L. E., M., Ragni, D., Scarano, F., Ferreira, C. S., Bussel, G. (2015). Tip-vortex instability and turbulent mixing in wind-turbine wakes. *Journal of Fluid Mechanics*, 781, 467–493. DOI 10.1017/jfm.2015.470.
11. Odemark, Y., Fransson, J. (2013). The stability and development of tip and root vortices behind a model wind turbine. *Experiments in Fluids*, 54(9), 1591. DOI 10.1007/s00348-013-1591-6.
12. Rodriguez, S., Jaworski, J. (2016). The stability of tip vortices generated by a flexible wind turbine. *DFD16 Meeting of the American Physical Society*. vol. 61, no. 20, H6.00009, Portland, Oregon.
13. Mohamed, M. H. (2014). Aero-acoustics noise evaluation of h-rotor darrieus wind turbines. *Energy*, 65(1), 596–604. DOI 10.1016/j.energy.2013.11.031.
14. Klimchenko, V. (2015). Experimental study of the effects of blade treatments on the tip vortex characteristics. *DFD15 Meeting of the American Physical Society*. vol. 60, no. 21, D16.00005, Boston, Massachusetts.
15. Ning, Z., Yang, Z. (2013). An experimental investigation on the control of tip vortices from wind turbine blade. *The 51st AIAA Aerospace Sciences Meeting including the New Horizons Forum and Aerospace Exposition*. Grapevine, Texas. DOI 10.2514/6.2013-1104.
16. Abdulrahim, A., Anik, E., Ostovan, Y., Uzol, O. (2016). Effects of tip injection on the performance and near wake characteristics of a model wind turbine rotor. *Renewable Energy*, 88, 73–82. DOI 10.1016/j.renene.2015.11.030.
17. Lignarolo, L., Ragni, D., Ferreira, C. S., Bussel, G. (2015). Turbulent mixing in wind turbine and actuator disc wakes: experiments and POD analysis. *The 33rd Wind Energy Symposium, AIAA SciTech Forum*. Kissimmee, Florida. DOI 10.2514/6.2015-0223.
18. Bastine, D., Witha, B., Wächter, M., Peinke, J. (2014). POD analysis of a wind turbine wake in a turbulent atmospheric boundary layer. *Journal of Physics: Conference Series*, 524, 012153. DOI 10.1088/1742-6596/524/1/012153.
19. Sirovich, L. (1987). Turbulence and the dynamics of coherent structures. I-Coherent structures. II-Symmetries and transformations. III-Dynamics and scaling. *Quarterly of Applied Mathematics*, 45(3), 561–571. DOI 10.1090/qam/910462.
20. Huang, G., Lu, W., Zhu, J., Fu, X., Wang, J. (2017). A nonlinear dynamic model for unsteady separated flow control and its mechanism analysis. *Journal of Fluid Mechanics*, 826, 942–974. DOI 10.1017/jfm.2017.321.